Triaxial tests in Fontainebleau sand

Latini, Chiara; Zania, Varvara

Publication date:
2016

Document Version
Publisher's PDF, also known as Version of record

Technical University of Denmark

Internal Report

Triaxial Tests in Fontainebleau Sand

Ph.D Student Chiara Latini

supervised by
Associate Professor Varvara Zania

July 10, 2017

Contents

Chapter 1

Introduction

The purpose of this internal report is to examine the influence of the relative density on the strength and deformation characteristics of Fontainebleau sand. Compression triaxial tests were performed on saturated sand samples with different densities and initial confining pressure σ'_r. Note that the testing procedure and the data processing were carried out according to the specifications of ETCS-F1.97. The internal report is divided into two chapters and four appendices associated with the results of chapter 2 are placed at the end of the report.

Chapter 2

Data processing

2.1 Introduction

Test setup

In Figure 2.1 the setup of a sample in the triaxial test can be seen. The sample, which has to be set dry, is packed in a cylindrical latex membrane with a flat, circular metal plate (pressure head) closing off the top and bottom ends. The cylinder (length l=7cm and diameter d=7cm) is placed into a bath of a hydraulic fluid (water), to provide pressure along the sides of the cylinder. The top plate is mechanically driven up or down along the axis of the cylinder to apply pressure on the sample. The distance that the upper plate travels is measured as a function of the force required to move it, as the pressure of the surrounding water is carefully controlled. The net change in volume of the sample is also measured, by the amount of water flowing in or out of the sample's pores. Once the chamber is filled with water, the sample can be saturated. The water flows through the sample with the siphon-principle by connecting the lower pressure head with a de-aired water container and the upper pressure head with a drain hose, respectively.

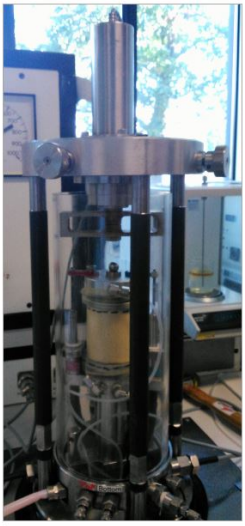

Figure 2.1: Setup of a test.

Measured parameters

The parameters measured in the triaxial test are the axial displacement ΔH, the height of the sample using LVDT's, the change in volume ΔW_{water} by the amount of water flowing in or out the sample, the chamber pressure σ_r and the axial load applied by the piston on the upper pressure head $\sigma_a - \sigma_r$.

Sand type

The sand type deployed in the triaxial tests is a Fontainebleau sand. Fontainebleau sand is a well-sorted, clean sand with a particle size ranging from $0.063mm$ to $0.25mm$, and a uniformly index of $U < 2$. Further classification parameters are given in Table 2.1 and they have been determined according to Dansk geoteknisk forening (DGF)-Bulletin 15 (2001).

Relative grain density	d_s	2.655
Densest deposition	e_{min}	0.549
Loosest deposition	e_{max}	0.853

Table 2.1: Classification parameters for sand

Experimental series

Samples at various relative densities I_D were tested in drained and undrained triaxial compression conditions after having been isotropically consolidated (CID-CUD) to various cell pressures σ'_r. The shear phase is done under both drained and undrained conditions. The axial deformation rate is $\varepsilon'_a = 1\%/$ hour. At approximately 50% of the expected peak deviatoric stress, q_{peak}, an unloading and reloading cycle was performed after which the sample was loaded in displacement control to full failure (approximately 15% axial strain ε_a). The test series is summarized in Table 2.2. Note that the relative density for the test series performed in undrained conditions cannot be determined, since the samples are looser than the loosest deposition, see Table 2.2.

2.2 Measurement corrections

Calculation of axial and volumetric strains requires accurate estimation of the initial height and area of the sample thus, corrections of the data have to be performed. According to the specifications of ETCS-F1.97 several corrections on the geometry of the samples have been applied for processing the data. The height and volume of sample after consolidation are given as:

$$H_c = H_0(1 - \varepsilon_a) \tag{2.1}$$

$$V_c = V_0 - \Delta V_c \tag{2.2}$$

where $\Delta V_c = \Delta W_{water}/\varrho_{water}$. The axial and volumetric strain should be calculated, initializing the variations of height and volume at the beginning of the shearing phase. Thus, they are corrected according to:

$$\varepsilon_a = \frac{\Delta H}{H_c} \tag{2.3}$$

Nr. Test	$\sigma_r^{'}$	**Relative Density** I_D	e_0
Test 1-CID	$50kPa$	0.53	0.699
Test 2-CID	$100kPa$	0.50	0.708
Test 3-CID	$200kPa$	0.57	0.684
Test 4-CID	$50kPa$	0.66	0.655
Test 5-CID	$100kPa$	0.65	0.660
Test 6-CID	$200kPa$	0.65	0.660
Test 7-CID	$50kPa$	0.80	0.612
Test 8-CID	$100kPa$	0.80	0.612
Test 9-CID	$200kPa$	0.80	0.612
Test 1-CUD	$100kPa$	$*$	0.856
Test 2-CUD	$50kPa$	$*$	0.844
Test 3-CUD	$100kPa$	$*$	0.921
Test 4-CUD	$50kPa$	$*$	0.908
Test 5-CUD	$100kPa$	$*$	0.901
Test 6-CUD	$50kPa$	$*$	0.920
Test 7-CUD	$50kPa$	$*$	0.877

Table 2.2: Experimental series in the triaxial apparatus

$$\varepsilon_v = \frac{\Delta V}{V_c} \tag{2.4}$$

Note that the area of the sample has to be corrected in order to calculate the axial stress for shearing phase:

$$A = \frac{1 - \varepsilon_v}{1 - \varepsilon_a} A_c \tag{2.5}$$

where $A_c = V_c / H_c$.

Chapter 3

Results

3.1 Consolidation phase

The bulk modulus K is a measure the compressibility of the sand. It is estimated during the consolidation phase as the slope of the axial stress p versus volumetric strain ε_v plot. Therefore it can be calculated according to:

$$\frac{\delta p}{\delta \varepsilon_v} = K \tag{3.1}$$

The bulk modulus for all drained triaxial tests is listed in Table 3.1.

Test	K
Test 1-CID	27.6MPa
Test 2-CID	38.0MPa
Test 3-CID	43.7MPa
Test 4-CID	30.9MPa
Test 5-CID	42.5MPa
Test 6-CID	43.0MPa
Test 7-CID	38.5MPa
Test 8-CID	43.9MPa
Test 9-CID	55.3MPa

Table 3.1: Bulk modulus K for all drained triaxial tests.

When the relative density of the sand is increased the sample becomes less compressible and hence a higher bulk modulus is expected. Also, for higher values of the confinement pressure it is expected that K will increase due to the increase in the radial pressure. The results seem to confirm this trend. The lowest bulk modulus was found for the Test 1, which has the lowest relative density and initial confining pressure. The highest bulk modulus was recorded for Test 9, which has the highest cell pressure and relative density, as it is expected.

3.2 Elasticity parameters

The elastic stiffness parameters of the soil are obtained from the shearing phase of the test. Depending on the plot the gradient in this phase will give Young's

Modulus, E, the shear Modulus, G, and Poisson's ratio, υ. The shear modulus is given as the slope of the deviatoric stress, δq versus the shear strain $\delta\varepsilon_q$ diagram describing the material's response to shear stress:

$$\frac{\delta q}{\delta \varepsilon_q} = 3G \tag{3.2}$$

Young's Modulus describes the resistance of the sand when it is deformed elastically. It is given as the slope of the deviatoric stress δq versus the axial strain $\delta\varepsilon_a$:

$$\frac{\delta q}{\delta \varepsilon_a} = E \tag{3.3}$$

Both E and G can be estimated theoretically from the initial shearing of the sample, E_i and G_i, when only elastic deformations occur. Hence E_i and G_i should be equal respectively to E and G, if the measurements of the triaxial setup are accurate in the low strains regime. The secant moduli E_{50} and G_{sec} are derived as the slope of

$$\frac{\delta q_{max,50}}{\delta \varepsilon_a} = E_{50} \tag{3.4}$$

$$\frac{\delta q_{max,50}}{\delta \varepsilon_q} = 3G_{sec} \tag{3.5}$$

where $q_{max,50}$ is 50% of the expected maximum stress value. Poisson's ratio υ, can be evaluated by plotting the ε_a and ε_r, where ε_r is the radial strain. For the estimation of υ the unloading and reloading phase is deployed and Poisson's ratio is given as follows:

$$\frac{\delta \varepsilon_r}{\delta \varepsilon_a} = \upsilon \tag{3.6}$$

The expected values for the Poisson's ratio is in the order of $[0.20; 0.30]$.

3.2.1 Unloading-reloading phase

The unloading and reloading modulus is the average slope of the unloading and reloading curve and it can readily be determined using the data from triaxial tests. In Appendix A the Young modulus E_{ur}, shear modulus G_{ur} and Poisson's ratio υ_{ur} at the loading and reloading phase are shown with respect to strains for each test.
In Table 3.2 the unloading and reloading parameters for all tests are listed.

Test	E_{ur}	G_{ur}	υ_{ur}
Test 1-CID	160.2MPa	68.8MPa	0.41
Test 2-CID	127.3MPa	42.8MPa	0.43*
Test 3-CID	278.1MPa	105.4MPa	0.35
Test 4-CID	251.9MPa	151.3MPa	–
Test 5-CID	151.4MPa	56.6MPa	0.42
Test 6-CID	268.0MPa	105.9MPa	0.34
Test 7-CID	424.0MPa	264.0MPa	–
Test 8-CID	187.3MPa	73.9MPa	0.39
Test 9-CID	269.2MPa	110.6MPa	0.36

Table 3.2: Young modulus E_{ur}, shear modulus G_{ur} and Poisson's ratio υ_{ur} for all drained triaxial tests.

Duncan et al. (1970) showed that E_{ur} and G_{ur} increase with increases in the confining pressure, but they are independent of the stress level. This pattern is recorded for loose and dense sand samples, respectively Test 1,3, Test 4,6 and Test 8,9.
In addition, it is noticed that the moduli tends to be higher if the particle are closely packed (dense samples). This is evident by comparing the outcomes of Test 1,4 and Test 2,5,8. Consequently, it is expected that the highest value of E_{ur} and G_{ur} is reached in Test 9, where we have the highest initial confining pressure and relative density. However, Test 7 has showed the maximum value of E_{ur} and G_{ur}.
Poisson's ratio obtained from the unloading and reloading phase attains higher values than those expected for drained sandy samples. In Test 3, Poisson's ratio cannot be estimated graphically, hence it is obtained according to:

$$G = \frac{E}{2(1+\upsilon)} \tag{3.7}$$

A graphical estimation of Poisson's ratio in Test 4 is not feasible. Due to the high shear modulus value, the numerical calculations resulted in a negative value and was not considered as a reliable result for Poisson's ratio, since that would be physically impossible. Furthermore, in Test 7 the estimation of Poisson's ratio cannot be considered reliable, due to the positive slope of the trendline of the unloading/reloading line in ε_r and ε_a.
No clear trend is seen for the Poisson's ratio in terms of confinement pressure or relative density. It is observed a small decrease in Poisson's ratio for samples with the same relative density, when the confining pressure increases. In terms of relative density it would be expected to see an increase in Poisson's ratio with increasing relative density; however the outcomes do not indicate this trend.

3.2.2 Initial moduli

The initial modulus is applicable only to very small deformations. Tatsuoka et al. (1997), Cuccovillo and Coop (1997) and Hoque and Tatsuoka (2004) showed that the deformation characteristics of sand samples are linear and elastic at strains of less than approximately 0.001%. In addition, the small-strain measurement requires relatively high accuracy. Therefore a significant small strain interval $\varepsilon_a = [0; 3e^{-4}]$ has been considered for the estimation of the initial moduli. The initial Young modulus E_i, shear modulus G_i and Poisson ratio υ_i are calculated and reported for each test in Appendix B. In Table 3.3 the initial elastic parameters for all drained triaxial tests are listed.

Test	E_i	G_i	υ_i
Test 1-CID	24.7MPa	8.13MPa	0.48
Test 2-CID	24.4MPa	8.13MPa	–
Test 3-CID	69.9MPa	59.5MPa	–
Test 4-CID	45.1MPa	19.8MPa	0.20
Test 5-CID	19.3MPa	3.9MPa	–
Test 6-CID	110.1MPa	30.6MPa	0.29
Test 7-CID	13.2MPa	5.1MPa	0.30
Test 8-CID	85.8MPa	29.6MPa	0.44
Test 9-CID	13.4MPa	9.0MPa	0.22

Table 3.3: Young modulus E_i, shear modulus G_i and Poisson's ratio υ_i for all drained triaxial tests.

Young's modulus E_i and shear modulus G_i are generally similar, see Test 1 and 2. This might be explained by the fact that the volumetric strains are near constant in the low strains range.
In addition, the value of Poisson's ratio is not feasible for Test 2,3 and 5, since Poisson's ratio cannot overcome 0.5 and then, it is not presented in Table 3.3. It can be stated that the outcomes in the low strain range are considerably scattered; therefore they are not reliable.

3.2.3 Secant moduli

The secant moduli are defined as the secant slope from the origin to a chosen point on the stress-strain curve. Note that the secant modulus does not respect the definition of elastic modulus in the classical elasticity theory, due to the fact that elastic deformation and plastic deformation develop simultaneously. In Table 3.4 the results of the secant moduli are listed for all drained triaxial tests. It is expected that the secant moduli increase by increasing the initial confining pressure $\sigma_r^{'}$. Results show this pattern. Regarding dense sands, Test 7 and 8 are characterized by similar outcomes. The outcomes further indicate that relative density has a considerably influence in E_{50} and G_{sec}. Indeed, secant moduli increases by increasing the relative density. The maximum value of E_{50} and G_{sec} is attained in Test 6 and it is not in agreement with the prevision. Hence, it is expected that the test with the highest confining pressure and relative density provides the maximum value of elastic moduli. Furthermore, it has been noticed

that $3G_{sec}$ and E_{50} are almost identical. This can be explained by the fact the influence of the volumetric strains is considerably small for the range of strain investigated.

Test	E_{50}	G_{sec}
Test 1-CID	17.0MPa	5.7MPa
Test 2-CID	22.6MPa	7.8Pa
Test 3-CID	43.2MPa	14.8MPa
Test 4-CID	22.3MPa	7.5MPa
Test 5-CID	27.7MPa	8.9MPa
Test 6-CID	86.3MPa	27.7MPa
Test 7-CID	32.9MPa	11.3MPa
Test 8-CID	33.2MPa	11.5MPa
Test 9-CID	60.4MPa	20.8MPa

Table 3.4: Young modulus E_{sec} and shear modulus G_{sec} for all drained triaxial tests.

It is of interest to note that Young's modulus E_{ur} can be calculated according to Marcher and Vermeer (2001) as follows:

$$E_{ur} = 4E_{50} \tag{3.8}$$

Equation 3.8 underestimates significantly Young's modulus E_{ur} particularly for loose and medium dense sand.

3.3 Estimation of strength parameters of CID tests

The experimental data included plots of deviatoric stress versus deviatoric strain, as well as volumetric strain versus deviatoric strain, for a range of different confining pressures and void ratios, see Figure 3.1, 3.2 and 3.3.

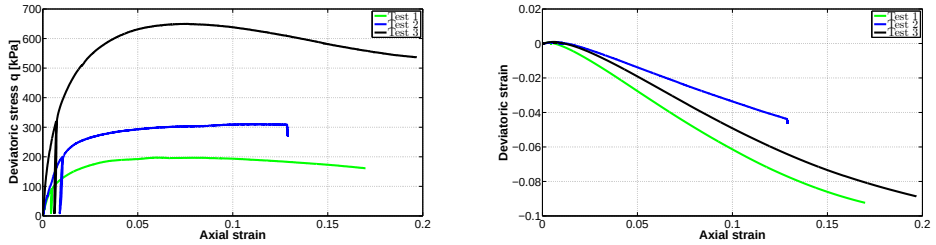

Figure 3.1: Variation of deviatoric stress versus axial strain and volumetric strain versus axial strain for Test 1, 2 and 3 (CID).

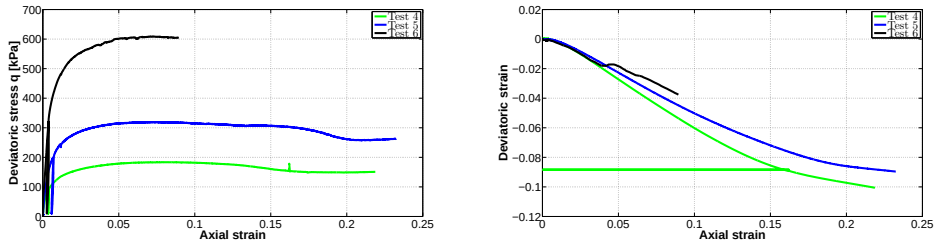

Figure 3.2: Variation of deviatoric stress versus axial strain and volumetric strain versus axial strain for Test 4,5 and 6 (CID).

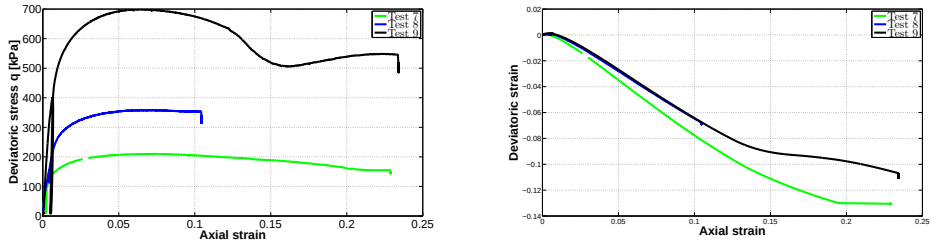

Figure 3.3: Variation of deviatoric stress versus axial strain and volumetric strain versus axial strain for Test 7,8 and 9 (CID).

The failure states in terms of p, q are used to determine the strength of the soil. The yield surface of Mohr-Coloumb criterion is presented in Equation 3.9.

$$q = Mp' + d \tag{3.9}$$

The strength characteristics of the soil are then the angle of friction φ and the cohesion c. The friction angle describes how well a soil sample can withstand shear stress. During shearing, the friction angle can be found as the angle between the normal force and the resultant force. While the cohesion c describes how a sample resists against a shearing deformation caused by a shear force. For $I_d = 0.5$ a friction angle between 30 ° and 35 ° is expected. For the sample of $I_d = 0.65$ the friction angle is expected to be higher and in the range of 35 ° and 40 °. For

dense sand samples ($I_d > 0.80$) an angle of friction in the interval of $[40°; 42°]$ is usually considered. At failure the mobilized friction angle (φ) reaches to its final value.

$$M = \frac{(6 \sin \varphi_f)}{(3 - \sin \varphi_f)} \tag{3.10}$$

The strength characteristics of this model can be obtained by plotting the failure states in terms of (p,q) and finding the best regression line to them. Therefore, the friction angle and the cohesion can be obtained as following:

$$\varphi_f = \sin^{-1}\left(\frac{3M}{6+M}\right) \tag{3.11}$$

$$c = \frac{d \tan(\varphi_f)}{M} \tag{3.12}$$

where d is the interecept of the failure line. No or very little cohesion in the order of $[0; 10]$kPa is expected. In Table 3.5 the stresses (p,q_{peak}) and the strains (ε_v,ε_q) at the failure are reported.

Test	q_{peak}	p	ε_q	ε_v
Test 1-CID	197.3kPa	114.8kPa	7.12e-2	-3.46e-2
Test 2-CID	310.8kPa	204.6kPa	1.23e-1	-3.76e-2
Test 3-CID	649.7kPa	415.8kPa	8.75e-2	-3.50e-2
Test 4-CID	183.7kPa	113.7kPa	9.56e-2	-4.73e-2
Test 5-CID	319.8kPa	205.2kPa	8.77e-2	-3.72e-2
Test 6-CID	558.9kPa	387.6kPa	8.05e-2	-2.80e-2
Test 7-CID	210.2kPa	120.9kPa	9.34e-2	-5.64e-2
Test 8-CID	358.8kPa	220.6kPa	8.36e-2	-4.27e-2
Test 9-CID	698.9kPa	434.2kPa	7.56e-2	-3.70e-2

Table 3.5: Stress and strains at the failure for all drained triaxial tests.

The results in Table 3.5 show that the peak of deviatoric stress increases from loose to dense sample by keeping the same initial confining pressure $\sigma_r^{'}$, as expected. Test 6 and Test 8 are characterized by an approximate value of the maximum deviatoric stress, since both triaxial tests did not reach 15% axial deformation. Table 3.6 shows the slope of the critical state line M and the angle of friction φ_f for each drained triaxial test.

Set	M	φ_f
Test 1-CID	1.72	41.0
Test 2-CID	1.52	37.3
Test 3-CID	1.56	38.2
Test 4-CID	1.61	39.8
Test 5-CID	1.56	38.0
Test 6-CID	1.50	37.0
Test 7-CID	1.74	42.4
Test 8-CID	1.62	39.8
Test 9-CID	1.61	39.4

Table 3.6: Failure line parameters for all drained triaxial tests.

In Table 3.7 the value of M coefficient (slope of the failure line), the angle of friction φ_f and the cohesion c at the failure are listed for all drained triaxial tests, gathered according to the same relative density. The failure line is shown in Figure 3.4, 3.5 and 3.6.

Set	I_D	M	φ_f	c
Test 1,2 and 3 (CID)	0.50	1.50	36.9	6.5kPa
Test 4,5 and 6 (CID)	0.66	1.50	36.9	9.5kPa
Test 7,8 and 9 (CID)	0.80	1.59	39.2	9.1kPa

Table 3.7: Failure line parameters for all drained triaxial tests.

The friction angle is larger for dense sand which is consistent, since the friction angle is greater if the sand is more compact. Indeed, the sand samples with high relative density are generally characterized by high friction angle, see both Table 3.6 and Table 3.7. It is evident that Test 1,2,3 and Test 4,5,6 are characterized by the same angle friction. It is expected that Test 1,2,3 provide lower friction angle, since they are loose sand samples.
In addition, the larger friction angle leads to a steeper slope in the Cambridge diagram, which results in a smaller intersection value, hence a smaller effective cohesion. This is not observed in the results achieved.

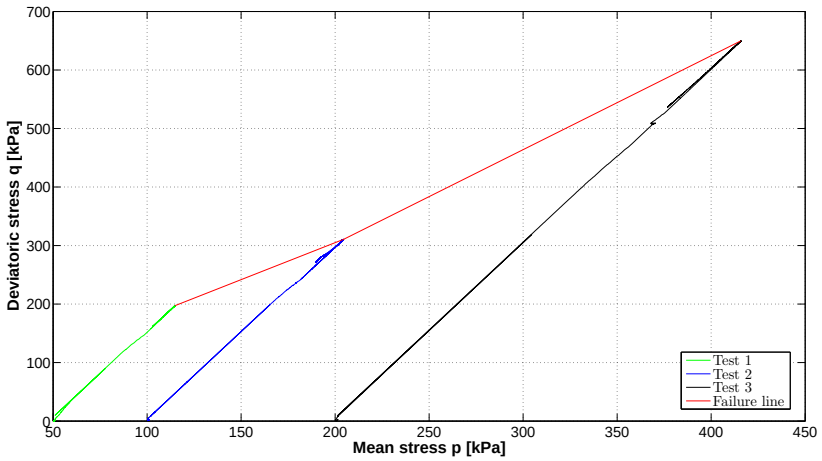

Figure 3.4: Failure line for Test 1,2 and 3 (CID)

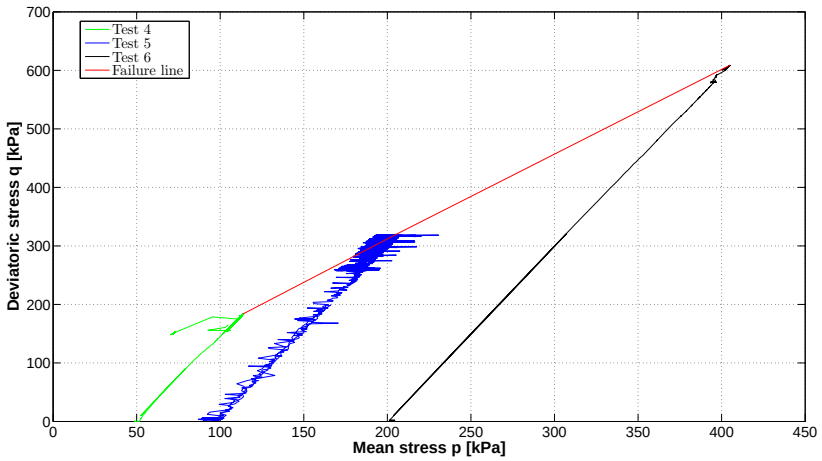

Figure 3.5: Failure line for Test 4,5 and 6 (CID)

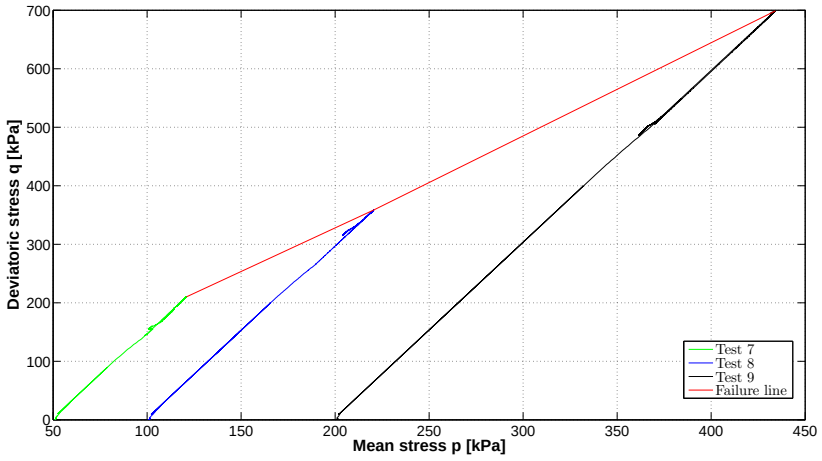

Figure 3.6: Failure line for Test 7,8 and 9 (CID)

3.4 Estimation of strength parameters of CUD tests

In Figure 3.7–3.12 pore pressure and deviator stress versus axial strain are shown for all the undrained tests. The pore pressure plotted with respect to axial strain shows a marked phase transformation from contraction (increase in pore pressure) to dilation (decrease in pore pressure) at about $2 - 2.5\%$ axial strain.

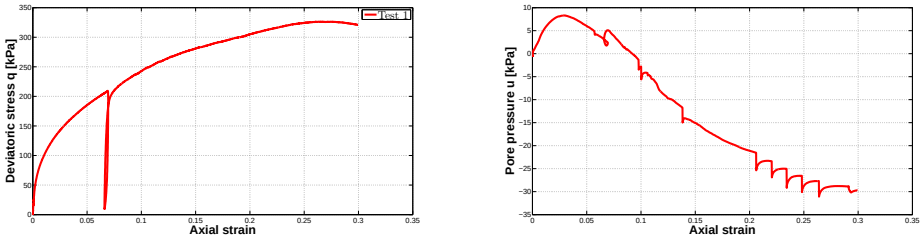

Figure 3.7: Variation of deviatoric stress versus axial strain and pore pressure versus axial strain for Test 1 (CUD).

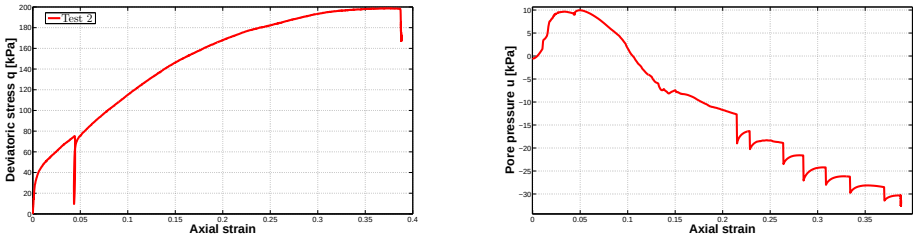

Figure 3.8: Variation of deviatoric stress versus axial strain and pore pressure versus axial strain for Test 2 (CUD).

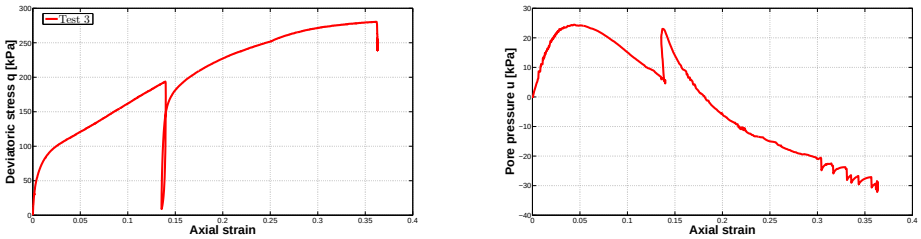

Figure 3.9: Variation of deviatoric stress versus axial strain and pore pressure versus axial strain for Test 3 (CUD).

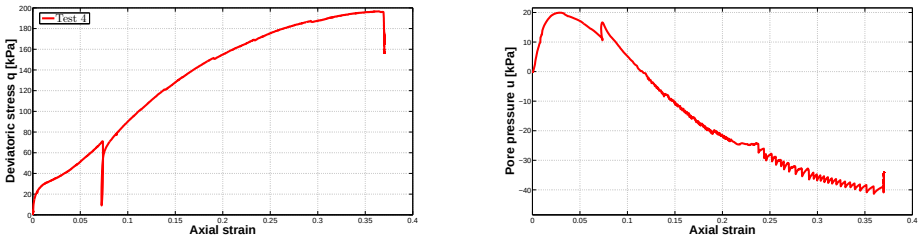

Figure 3.10: Variation of deviatoric stress versus axial strain and pore pressure versus axial strain for Test 4 (CUD).

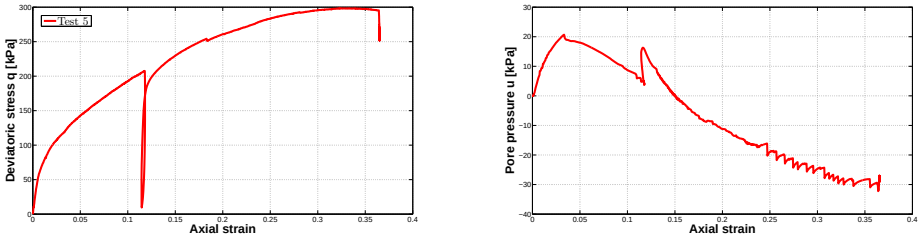

Figure 3.11: Variation of deviatoric stress versus axial strain and pore pressure versus axial strain for Test 5 (CUD).

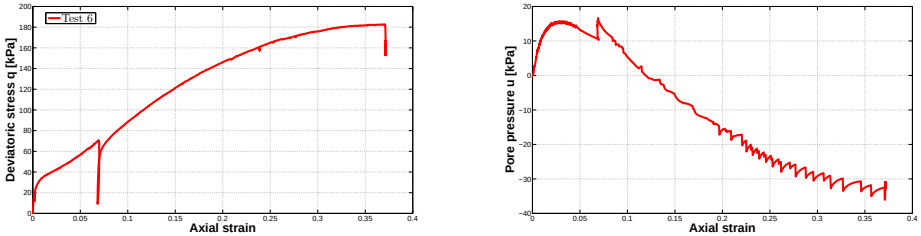

Figure 3.12: Variation of deviatoric stress versus axial strain and pore pressure versus axial strain for Test 6 (CUD).

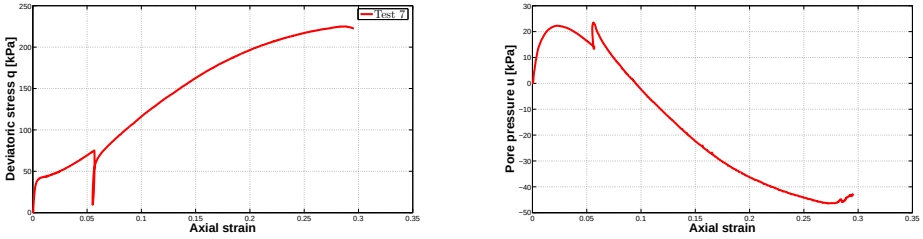

Figure 3.13: Variation of deviatoric stress versus axial strain and pore pressure versus axial strain for Test 7 (CUD).

While in Figure 3.14–3.17 the variation of the deviatoric stress q is illustrated with respect to the mean stress p for each undrained triaxial test.

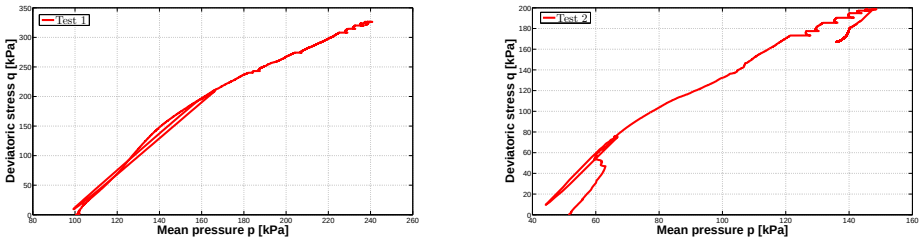

Figure 3.14: Variation of deviatoric stress versus mean stress for Test 1 and Test 2 (CUD).

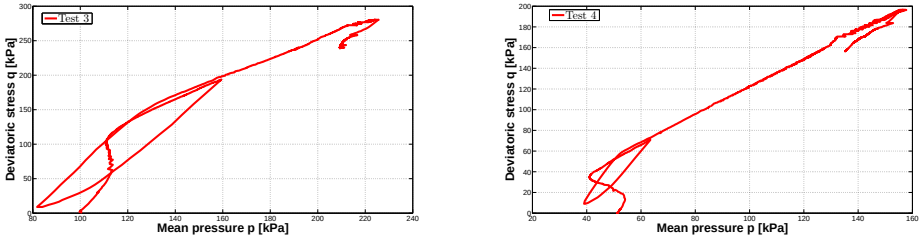

Figure 3.15: Variation of deviatoric stress versus mean stress for Test 3 and Test 4 (CUD).

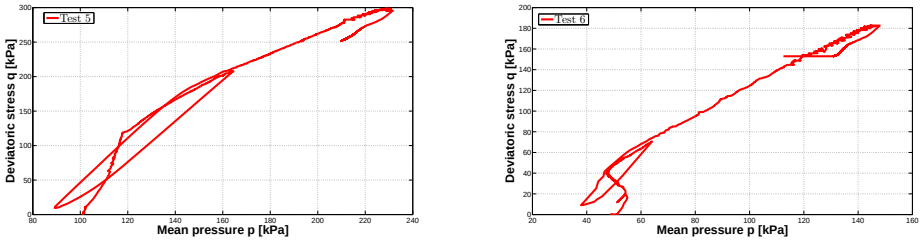

Figure 3.16: Variation of deviatoric stress versus mean stress for Test 5 and Test 6 (CUD).

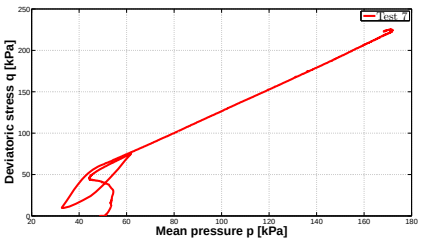

Figure 3.17: Variation of deviatoric stress versus mean stress for Test 7 (CUD).

The deviatoric and mean stress ($q_{failure}$, $p^{'}$) at failure are listed in Table 3.8. The results show that the deviatoric stress at failure increases from very loose to loose sample by keeping the same initial confining pressure $\sigma_r^{'}$, see Test 1,5,3 and Test 2,8,4,6. In Table 3.8 the value of M coefficient (slope of the failure line) and the angle of friction φ_f at the failure are also listed for all undrained triaxial tests.

Set	e_0	$q_{failure}$	$p^{'}$	M	φ_f
Test 1-CUD	0.856	144.4kPa	138.9kPa	1.04	26.3
Test 2-CUD	0.844	59.2kPa	60.3kPa	0.98	24.9
Test 3-CUD	0.921	104.0kPa	110.9kPa	0.94	24.0
Test 4-CUD	0.908	40.1kPa	42.9kPa	0.93	23.7
Test 5-CUD	0.901	120.3kPa	119.5kPa	1.01	25.6
Test 6-CUD	0.920	40.1kPa	47.2kPa	0.85	21.9
Test 7-CUD	0.877	43.7kPa	44.5kPa	0.98	24.9

Table 3.8: Failure line parameters for all undrained triaxial tests.

It is expected that the friction angle increases by increasing the relative density for same initial confining pressure $\sigma_r^{'}$. This trend is visible for Test 1,5,3 and Test 2,8,4,6. In addition, the angle of friction in all tests attains values lower than 30°, which is in agreement with the studies of Meyerhoff (1956) and Carter and Bentley (1991) for very loose sand samples. Furthermore, the maximum friction angle recorded is for the sand sample with higher relative density, see Test 2 for initial confining pressure $\sigma_r^{'} = 50kPa$ and Test 1 for initial confining pressure $\sigma_r^{'} = 100kPa$. Test 6 should be characterized by the minimum value of friction angle, since it has the highest void ratio for the smallest initial confining pressure in the tests' set. This is consistent with the outcome achieved for Test 6. In addition, the maximum value of the pore pressure and the relative stresses (u_{peak}, q, $p^{'}$) are reported in Table 3.9.

Set	e_0	$\sigma_r^{'}$	q	$p^{'}$	u_{peak}
Test 1-CUD	0.856	100kPa	133.0kPa	123.2kPa	8.1kPa
Test 2-CUD	0.844	50kPa	76.3kPa	66.5kPa	9.6kPa
Test 3-CUD	0.921	100kPa	112.0kPa	107.6kPa	24.4kPa
Test 4-CUD	0.908	50kPa	44.1kPa	41.9kPa	19.9kPa
Test 5-CUD	0.901	100kPa	131.1kPa	124.1kPa	20.7kPa
Test 6-CUD	0.920	50kPa	55.6kPa	52.7kPa	15.4kPa
Test 7-CUD	0.877	50kPa	51.7kPa	46.3kPa	22.3kPa

Table 3.9: Maximum pore pressure and relative stresses for all undrained triaxial tests.

3.5 Estimation of dilation angle

The dilation angle ψ is evaluated from the variation of volumetric strain versus the axial strain. Since the dilation angle is a measure of the volume change when the test is subjected to shear deformations, it should only be derived from the plastic strains:

$$\frac{\varepsilon_v}{\varepsilon_a} = -\frac{6\cos\psi}{3-\sin\psi} \tag{3.13}$$

The results are listed in Table 3.10 for all drained triaxial tests.

Test	I_D	σ_r	ψ
Test 1-CID	0.50	50kPa	15.7
Test 2-CID	0.50	100kPa	10.8
Test 3-CID	0.50	200kPa	9.0
Test 4-CID	0.66	50kPa	16.7
Test 5-CID	0.66	100kPa	14.2
Test 6-CID	0.66	200kPa	13.9
Test 7-CID	0.80	50kPa	22.1
Test 8-CID	0.80	100kPa	18.9
Test 9-CID	0.80	200kPa	17.9

Table 3.10: Dilation angle ψ for all drained traixial tests.

It is expected that the dilation angle ψ reduces by increasing the initial confining pressure $\sigma_r^{'}$. Looking at loose samples, the variation of dilation angle for Test 1, Test 2 and Test 3 with respect to the initial confining pressure is consistent. The same trend is observed for medium dense and dense samples, respectively Test 4,5,6 and Test 7,8,9.
In addition, the dilation angle should increase from loose to dense sands. For an initial confining pressure of $\sigma_r^{'} = 50kPa$, this pattern has been noticed by comparing ψ of Test 3 with that of Test 4 and Test 7. The variation of dilation angle with the relative density is consistent for all the test; even though the dilation angle of Test 7 and Test 8 is quite high. As a rule of thumb, sand sample having a friction angle above 30° will be characterized by a dilation angle approximately equal to $\varphi - 30°$, see Bolton (1984). This is seen not to be the case for the tests investigated.

3.6 Estimation of the critical state

The concept of the critical state is fundamental to understand the mechanical response of soil. The critical state has been defined as the state at which the soil "continues to deform at constant stress and constant void ratio" (Roscoe et al., 1958). The critical state is generally estimated from drained tests on dense sands. However the actual location of the line is difficult to assess. These difficulties are mainly due to experimental limitations and lack of accurate observations. Ultimate state generally takes place at large strains and these strains can sometimes exceed the limitations of a triaxial apparatus (Been et al., 1991). To solve the above-mentioned measurement problems, Castro (1969) performed undrained, stress-controlled triaxial tests on very loose sands to obtain a steady state line.

According to Poulos (1981), the steady state of deformation for any mass of particles is that state in which the mass is continuously deforming at constant volume, constant normal effective stress, constant shear stress, and constant velocity. Been et al. (1991) showed that the critical and steady state line are the same from a practical standpoint. Hence, the sample reaches the critical or steady state, when it will experience large strains under monotonic loading. Furthermore, it was proposed a unique critical state line (CSL) for each sand in an e$-logp^{'}$ plot which is independent of type of loading, sample preparation method and initial density.
In this study it is possible to detect the critical state in Test 5,7 and 9 (CID), see Figure 3.1, 3.2 and 3.3, since shearing occurs with no volume change. In regards to undrained conditions the occurrence of the critical state becomes visible in Test 1,4,5,6 and 7(CUD) as shown in Figure 3.7, 3.10, 3.11, 3.12 and 3.13.
Particularly, the critical state line can be obtained by plotting the results of triaxial compression tests at the critical state in p$-$q space and fitting a best fit line through the data points as shown in Figure 3.18a. In addition, the void ratio at the critical state e_{cr} can be estimated by plotting undrained triaxial tests data in eln($p^{'}_{cr}$) space and fit them to a line having expression as shown in Figure 3.18b. According to Been et al. (1991), this is a generally reasonable approximation for sub-angular or subrounded quartz sands in the stress range of $10-500$kPa, which is the case of the triaxial tests performed in this study.

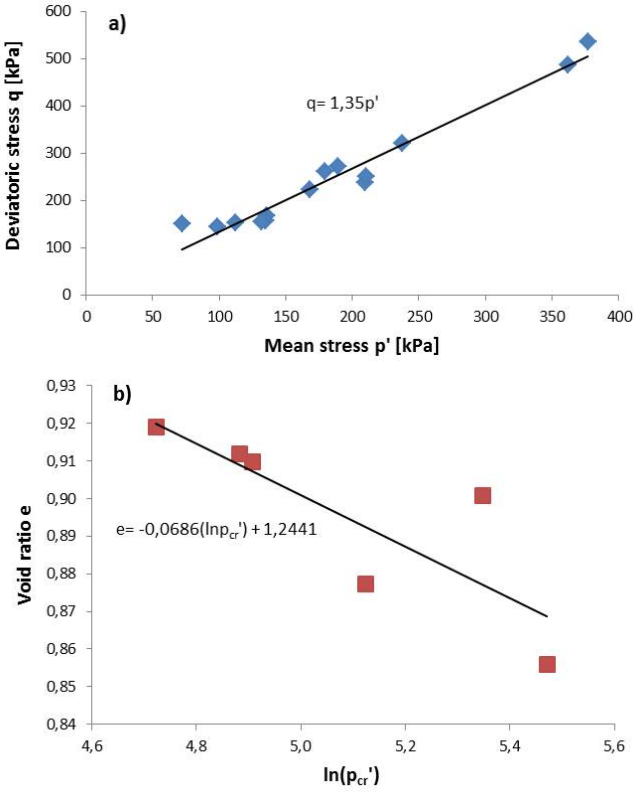

Figure 3.18: Critical state line in q-p (a) and e$-$ln($p^{'}_{cr}$) plane (b).

Chapter 4

Conclusions

The aim of this study was to present a series of triaxial tests carried out on Fontainebleau sand in order to investigate the influence of the relative density on the strength and deformation characteristics of this type of sand. In general the strength parameters found seemed sensible and within the range of what would be expected. For the elasticity parameters estimated in the unloading reloading phase no clear trend was seen for varying relative densities and confinement pressure.

References

Been, K., Jefferies, M. G. and Hachey, J. 1991. Critical state of sands. Geotechnique, 41(3), 365-381.

Bolton, M. D. 1984. The strength and dilatancy of sands. Cambridge University Engineering Department.

Carter, M. and Bentley, S. 1991. Correlations of soil properties. Penetech Press Publishers, London.

Castro, G. 1969. Liquefaction of sands. ph. D. Thesis, Harvard Soil Mech.

Cuccovillo, T. and Coop, M. 1997. Yielding and prefailure deformation of structured sands. Geotechnique, 47(3), 491-508.

Duncan, J.M. and Chang, C.Y. 1970. Nonlinear analysis of stress and strain in soils. Journal of Soil Mechanics, 96(5), 1629-1653.

Hoque, E. and Tatsuoka, F. 2004. Effects of stress ratio on small strain stiffness during triaxial shearing. Geotechnique, 54(7), 429-439.

Marcher, T. and P. A. Vermeer. Macromodelling of softening in non-cohesive soils. Continuous and discontinuous modelling of cohesive-frictional materials. Springer Berlin Heidelberg, 2001. 89-110.

Meyerhof, G. 1956. Penetration tests and bearing capacity of cohesionless soils. J Soils Mechanics and Foundation Division ASCE, 82(SM1).

Poulos, S. J. 1981. The steady state of deformation. Journal of Geotechnical and Geoenvironmental Engineering, 107(ASCE 16241 Proceeding).

Roscoe, K. H., Schofield, A., and Wroth, C. P. 1958. On the yielding of soils. Geotechnique, 8(1), 22-53.

Tatsuoka, F., Sato, T., Park, C., Kim, Y.S., Mukabi, J.N: and Kohata, Y. 1994a. Measurements of elastic properties of geomaterials in laboratory compression tests. Geotechnical Testing Journal, 17(1), 80-84.

Appendix A

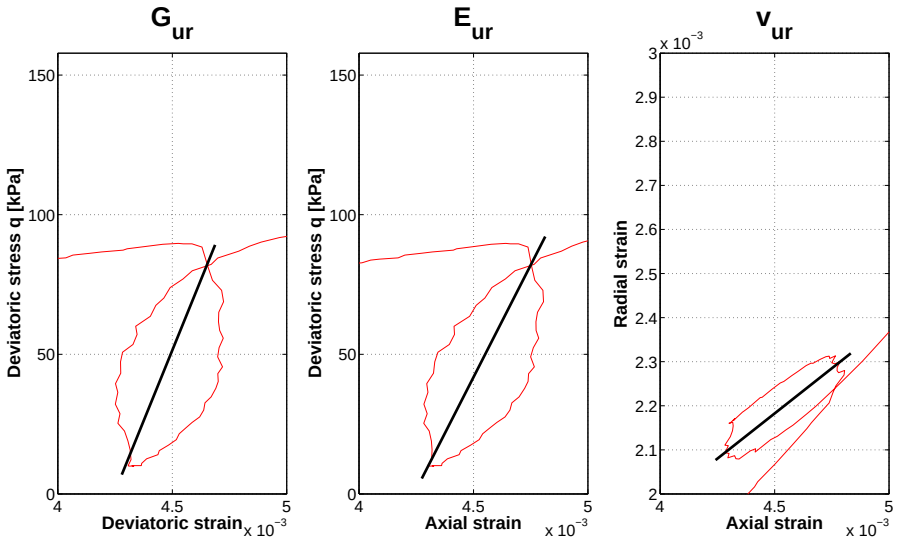

Figure 4.1: Young modulus E_{ur}, shear modulus G_{ur} and Poisson's ratio υ_{ur} at unloading and reloading phase for test 1 (CID).

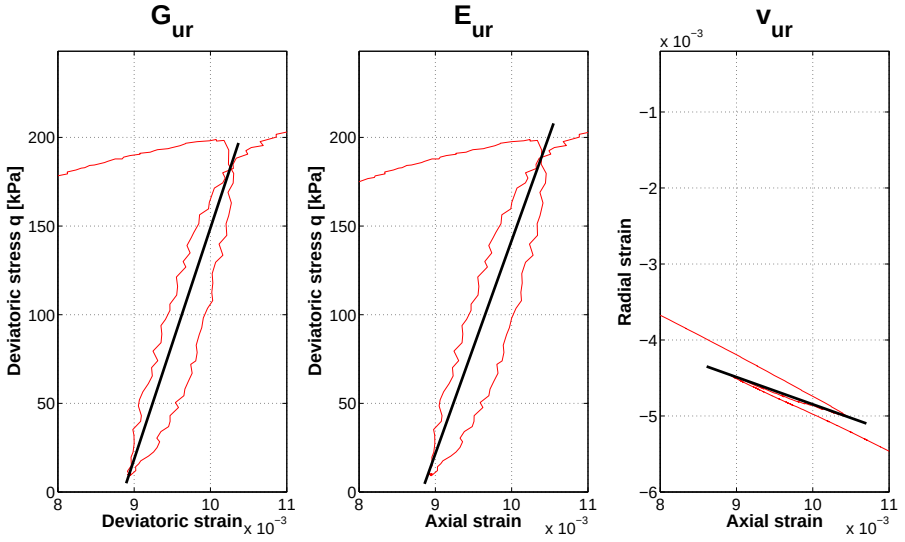

Figure 4.2: Young modulus E_{ur}, shear modulus G_{ur} and Poisson's ratio υ_{ur} at unloading and reloading phase for test 2 (CID).

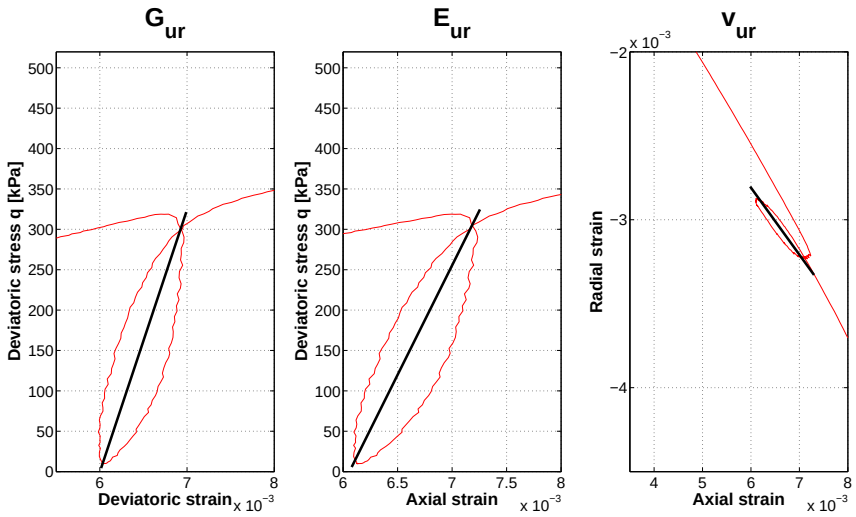

Figure 4.3: Young modulus E_{ur}, shear modulus G_{ur} and Poisson's ratio υ_{ur} at unloading and reloading phase for test 3 (CID).

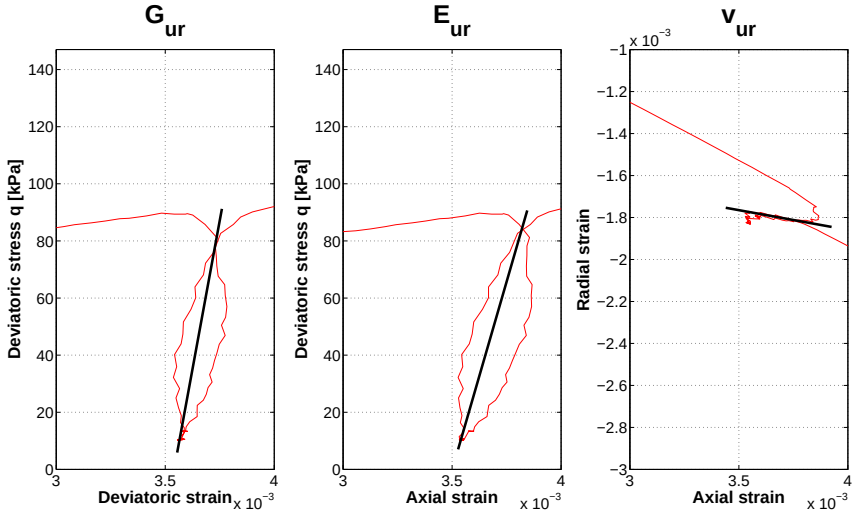

Figure 4.4: Young modulus E_{ur}, shear modulus G_{ur} and Poisson's ratio υ_{ur} at unloading and reloading phase for test 4 (CID).

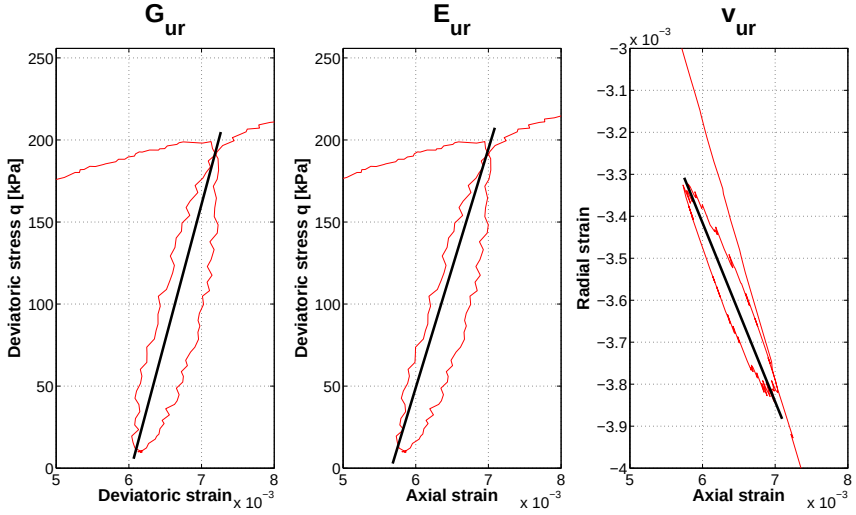

Figure 4.5: Young modulus E_{ur}, shear modulus G_{ur} and Poisson's ratio υ_{ur} at unloading and reloading phase for test 5 (CID).

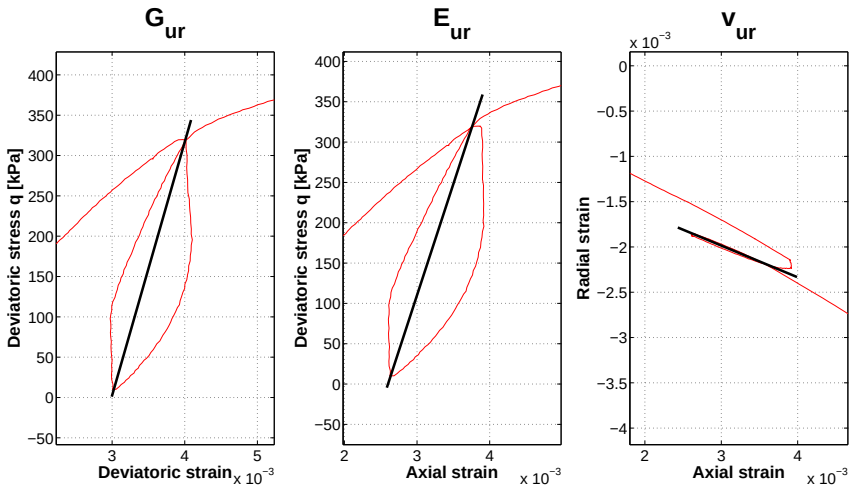

Figure 4.6: Young modulus E_{ur}, shear modulus G_{ur} and Poisson's ratio υ_{ur} at unloading and reloading phase for test 6 (CID).

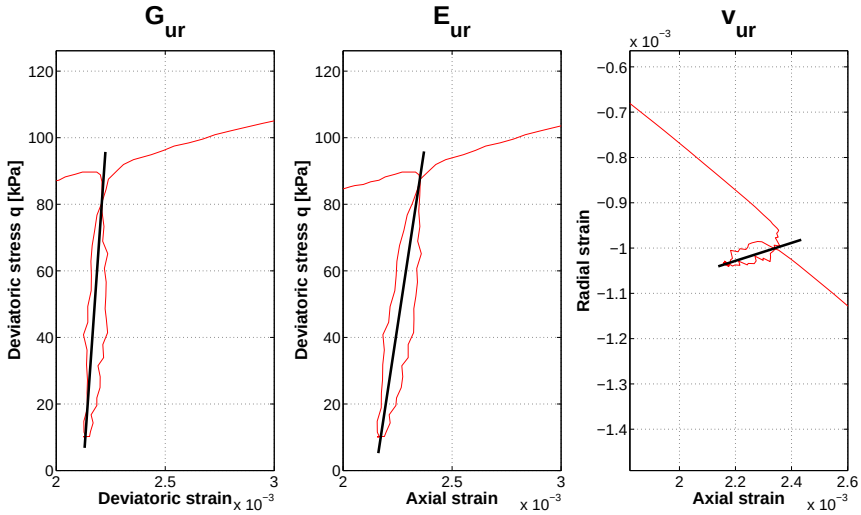

Figure 4.7: Young modulus E_{ur}, shear modulus G_{ur} and Poisson's ratio υ_{ur} at unloading and reloading phase for test 7 (CID).

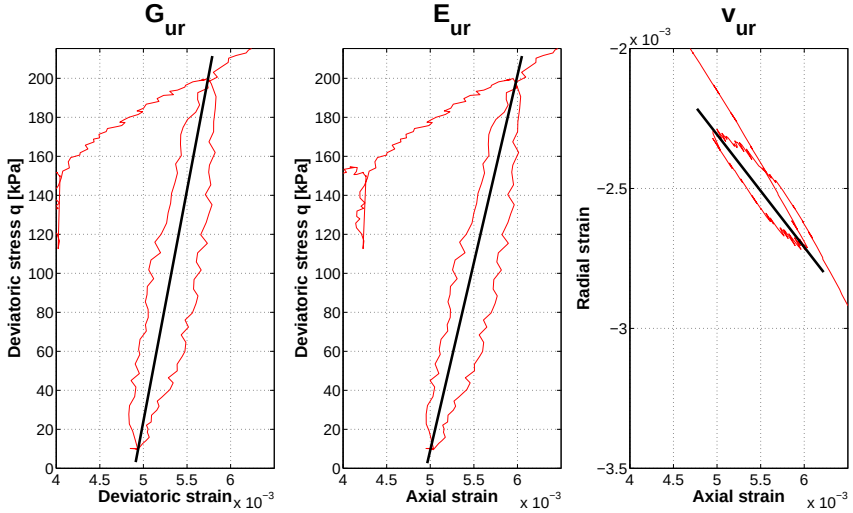

Figure 4.8: Young modulus E_{ur}, shear modulus G_{ur} and Poisson's ratio υ_{ur} at unloading and reloading phase for test 8 (CID).

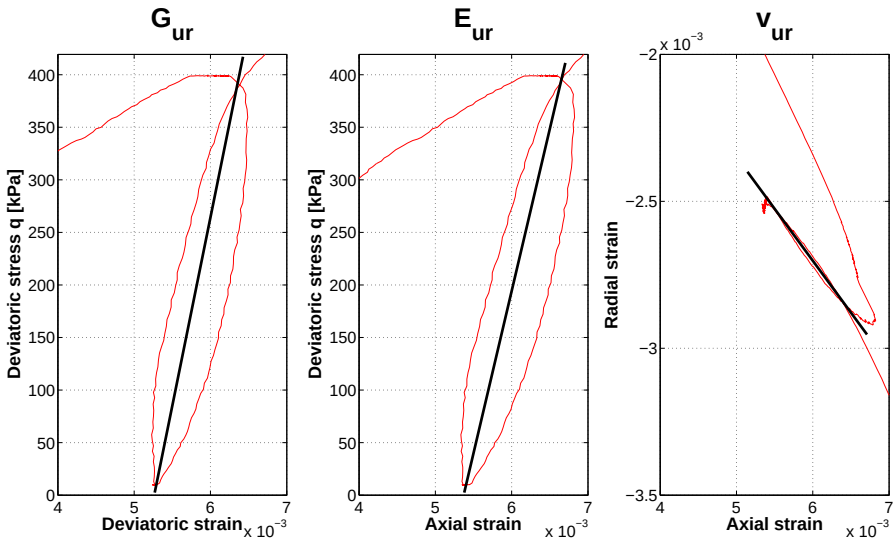

Figure 4.9: Young modulus E_{ur}, shear modulus G_{ur} and Poisson's ratio υ_{ur} at unloading and reloading phase for test 9-CID.

Appendix B

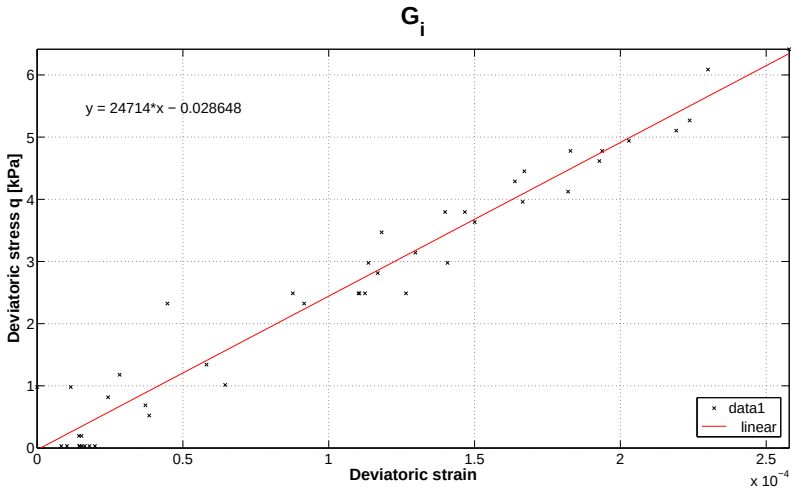

Figure 4.10: Initial Young modulus E_i for Test 1 (CID).

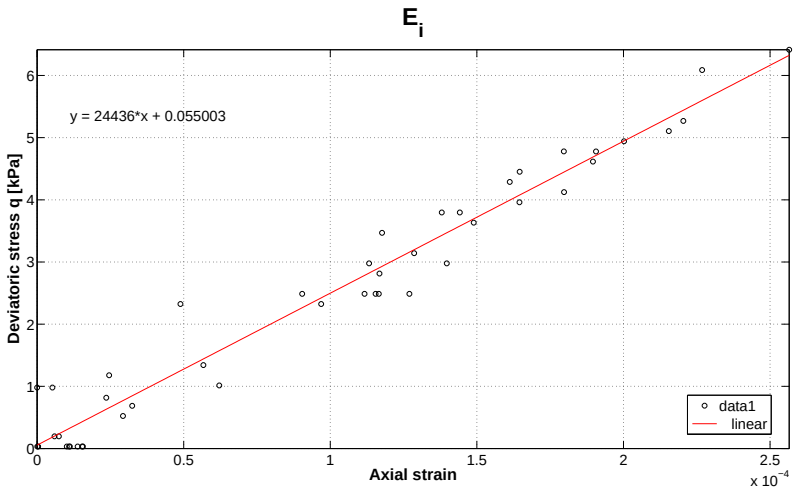

Figure 4.11: Initial shear modulus G_i for Test 1 (CID).

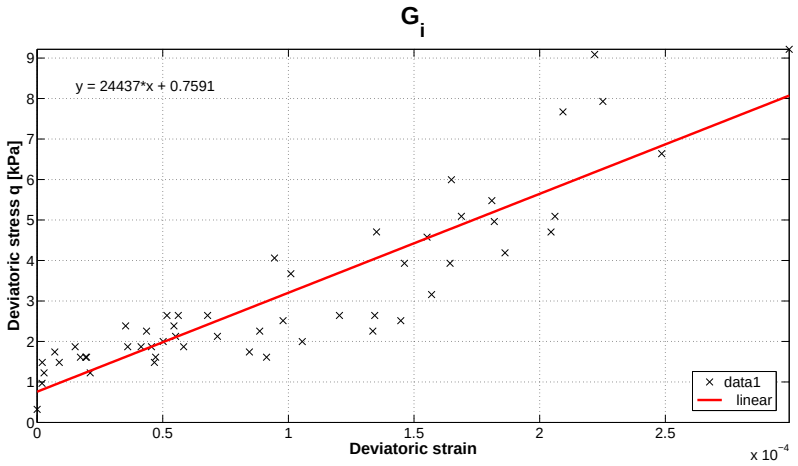

Figure 4.12: Initial Young modulus E_i for Test 2 (CID)..

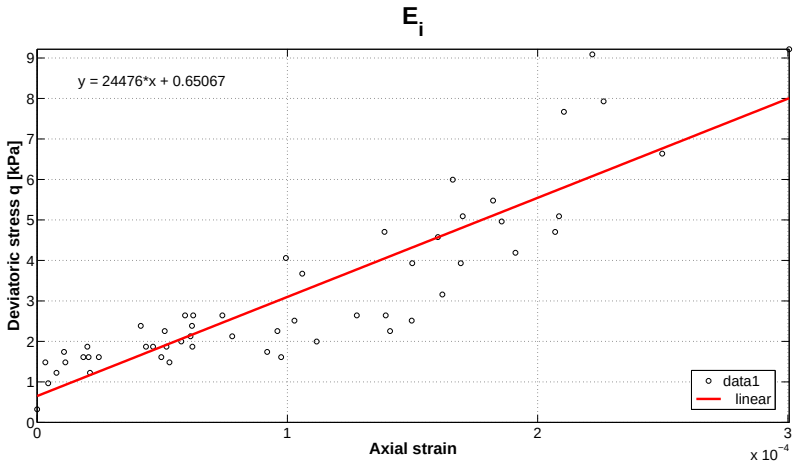

Figure 4.13: Initial shear modulus G_i for Test 2 (CID).

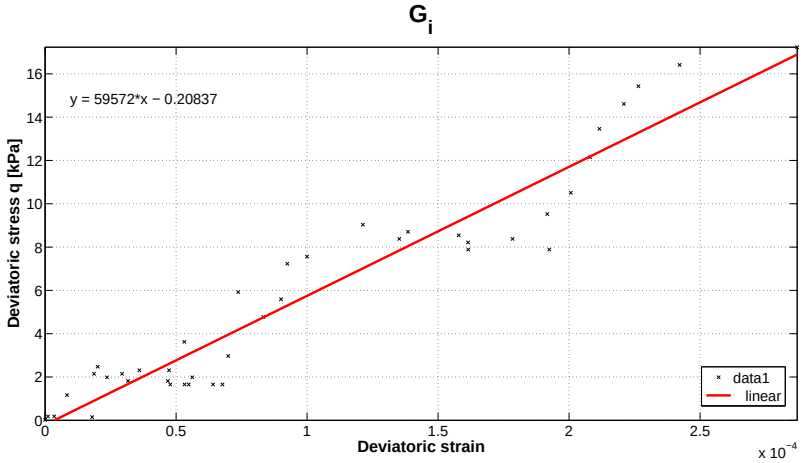

Figure 4.14: Initial Young modulus E_i for Test 3 (CID).

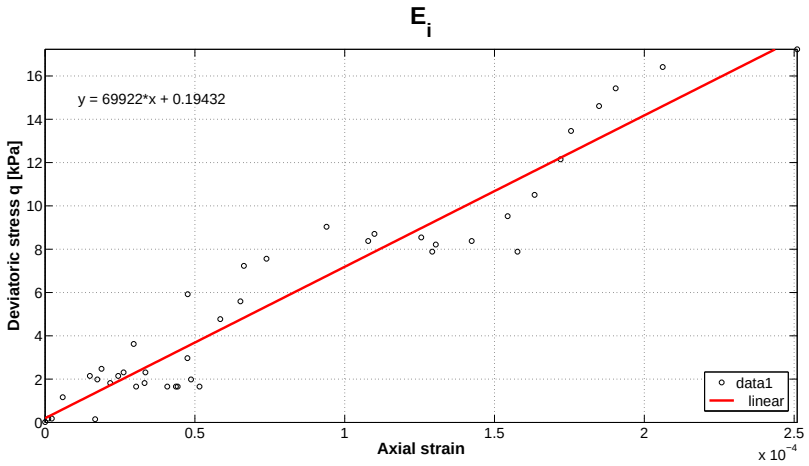

Figure 4.15: Initial shear modulus G_i for Test 3 (CID).

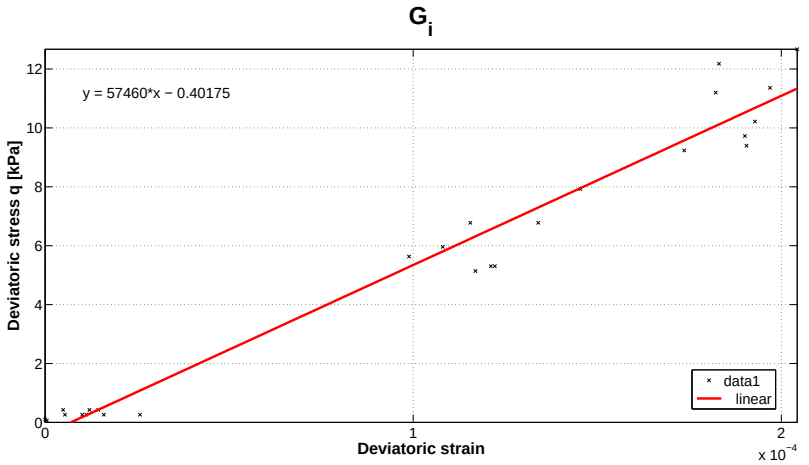

Figure 4.16: Initial Young modulus E_i for Test 4 (CID).

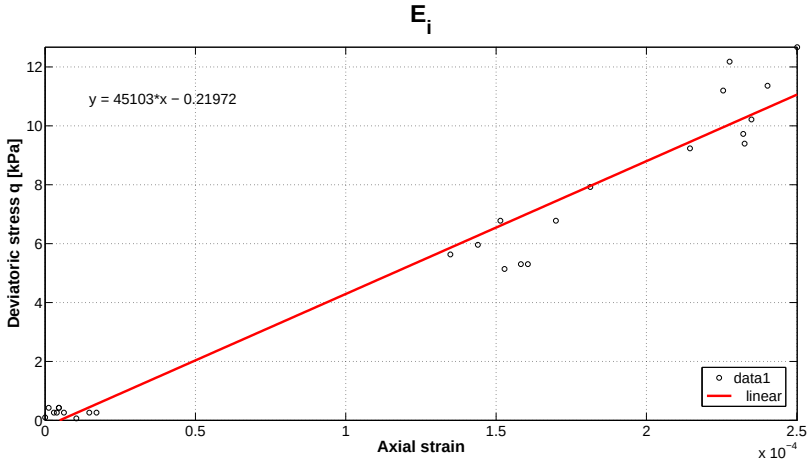

Figure 4.17: Initial shear modulus G_i for Test 4 (CID).

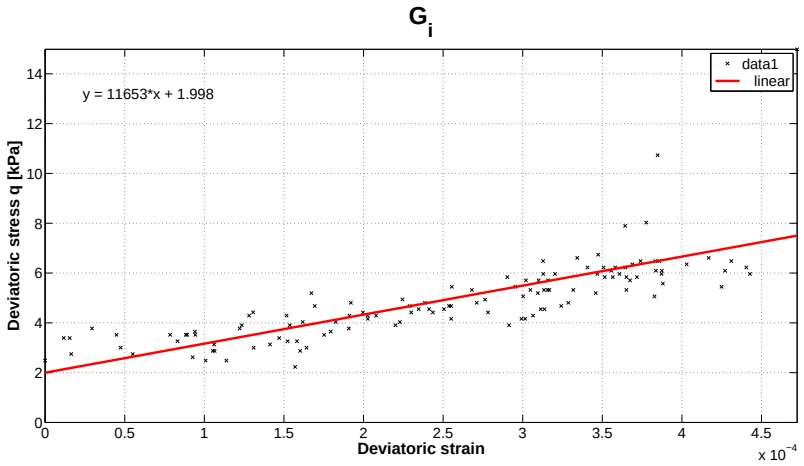

Figure 4.18: Initial Young modulus E_i for Test 5 (CID).

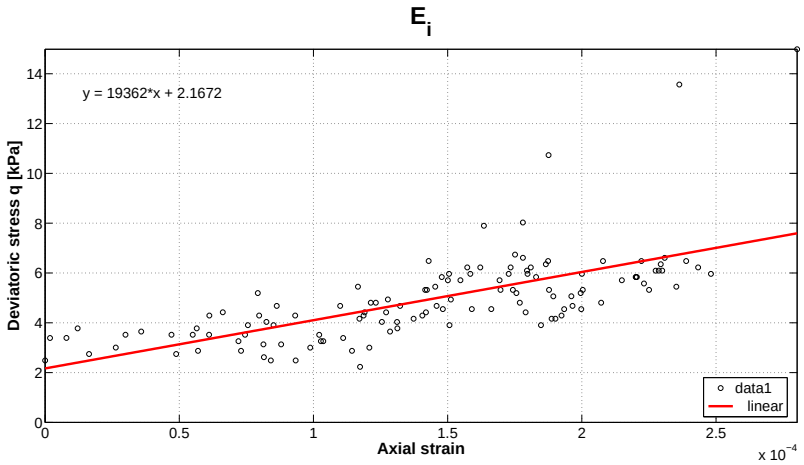

Figure 4.19: Initial shear modulus G_i for Test 5 (CID).

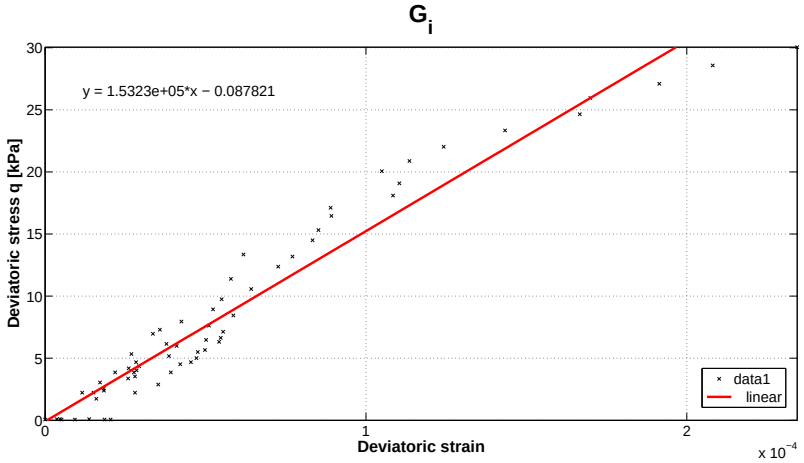

Figure 4.20: Initial Young modulus E_i for Test 7 (CID).

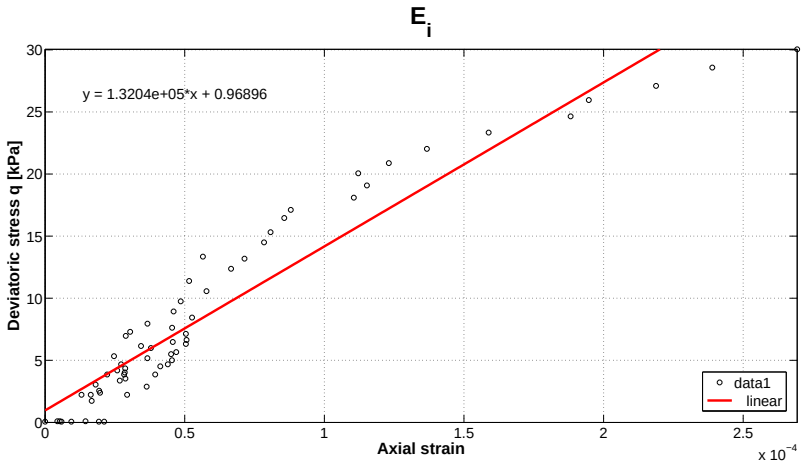

Figure 4.21: Initial shear modulus G_i for Test 7 (CID).

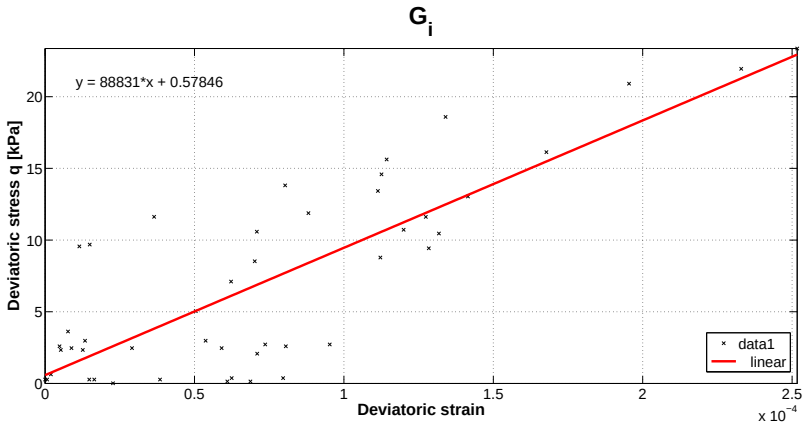

Figure 4.22: Initial Young modulus E_i for Test 8 (CID).

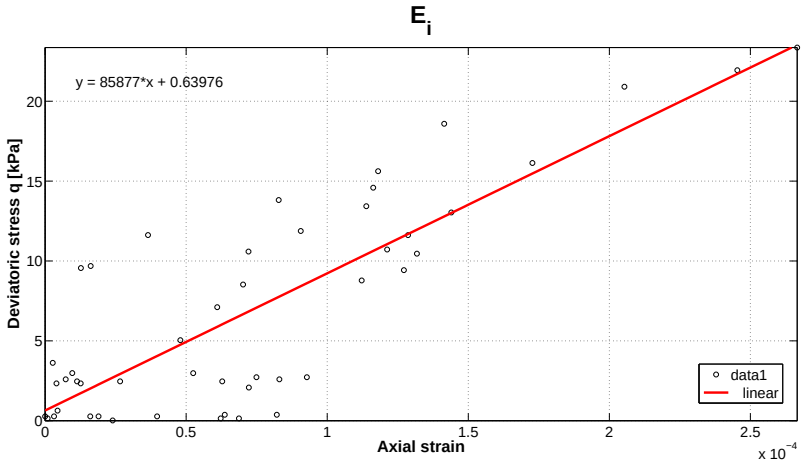

Figure 4.23: Initial shear modulus G_i for Test 8 (CID).

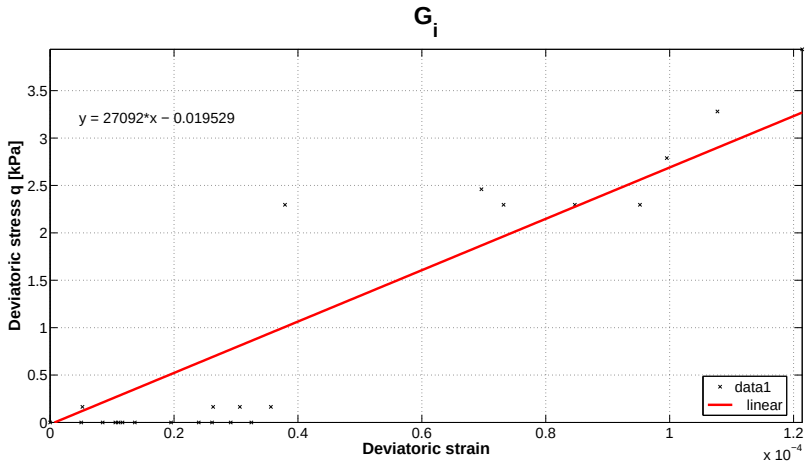

Figure 4.24: Initial Young modulus E_i for Test 9 (CID).

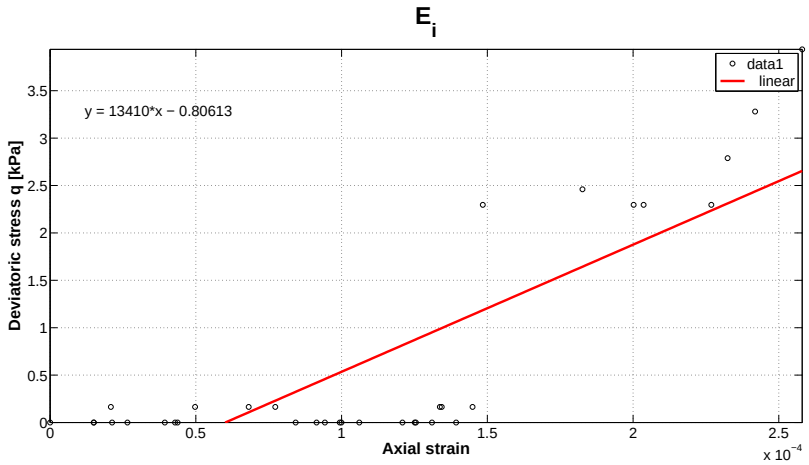

Figure 4.25: Initial shear modulus G_i for Test 9 (CID).

Appendix C

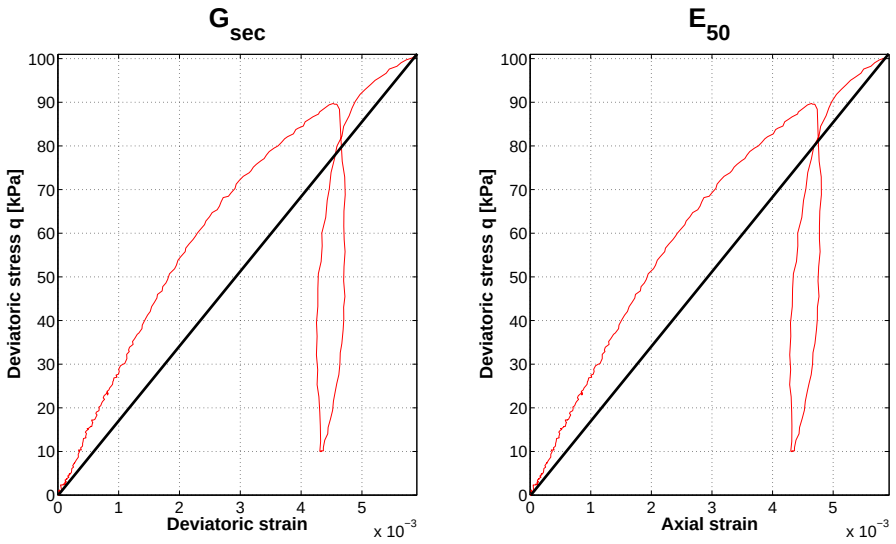

Figure 4.26: Young modulus E_{sec} and shear modulus G_{sec} for Test 1 (CID).

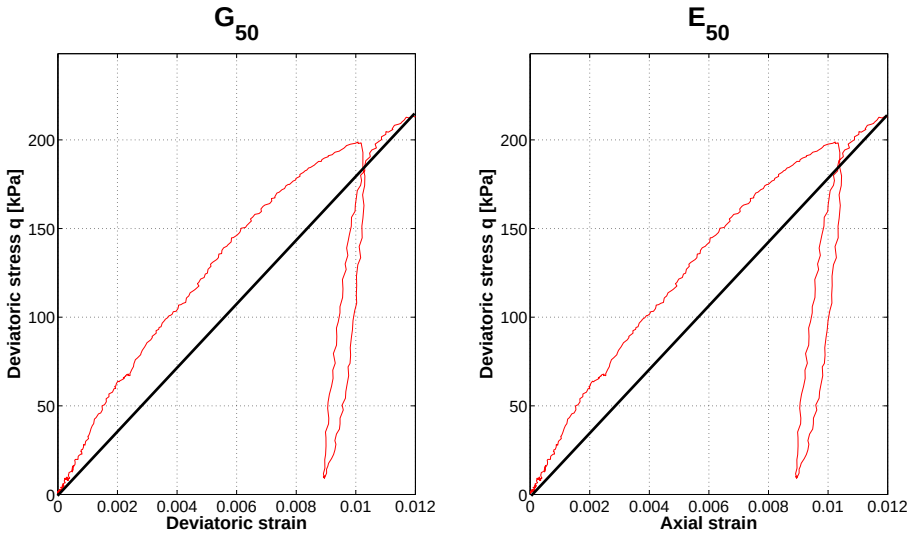

Figure 4.27: Young modulus E_{50} and shear modulus G_{sec} for Test 2 (CID).

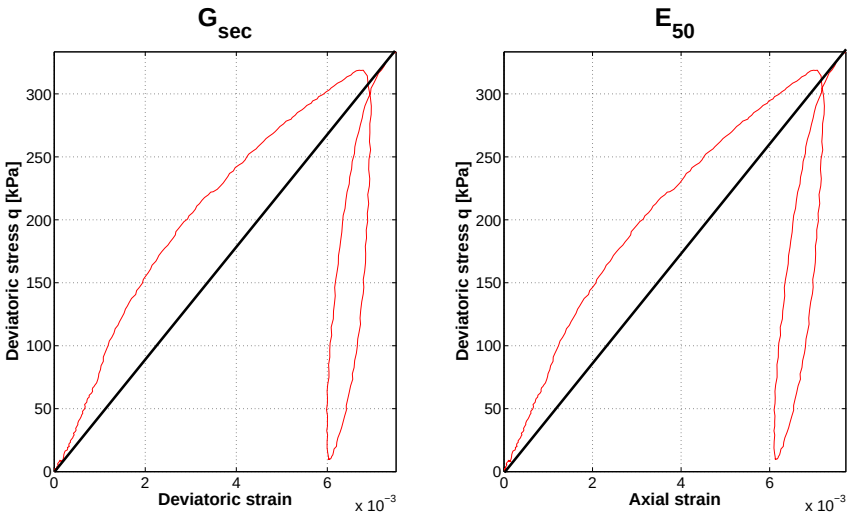

Figure 4.28: Young modulus E_{50} and shear modulus G_{sec} for Test 3 (CID).

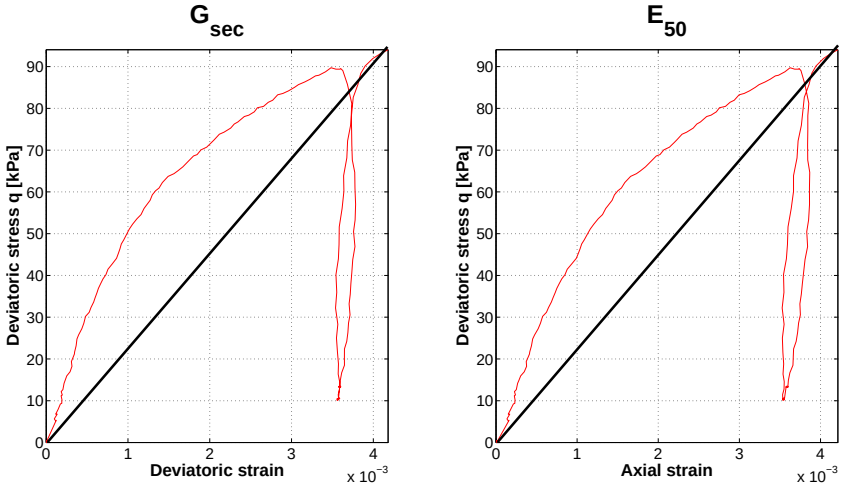

Figure 4.29: Young modulus E_{50} and shear modulus G_{sec} for Test 4 (CID).

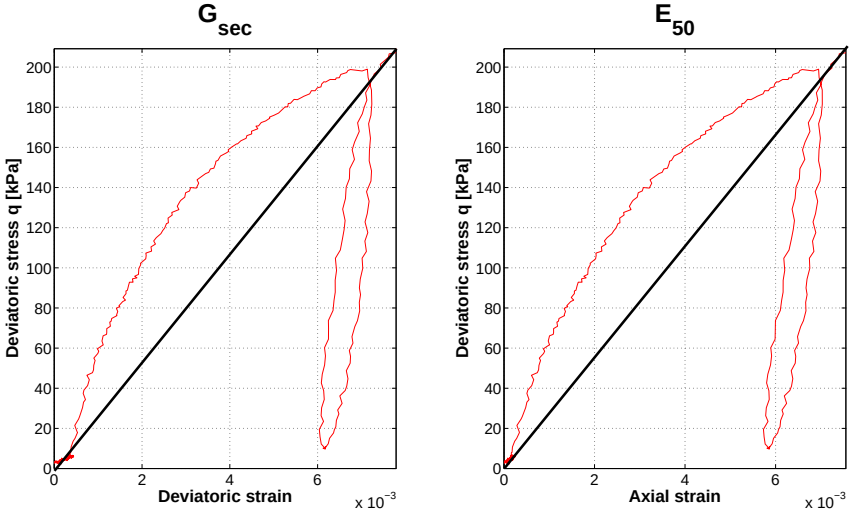

Figure 4.30: Young modulus E_{50} and shear modulus G_{sec} for Test 5 (CID).

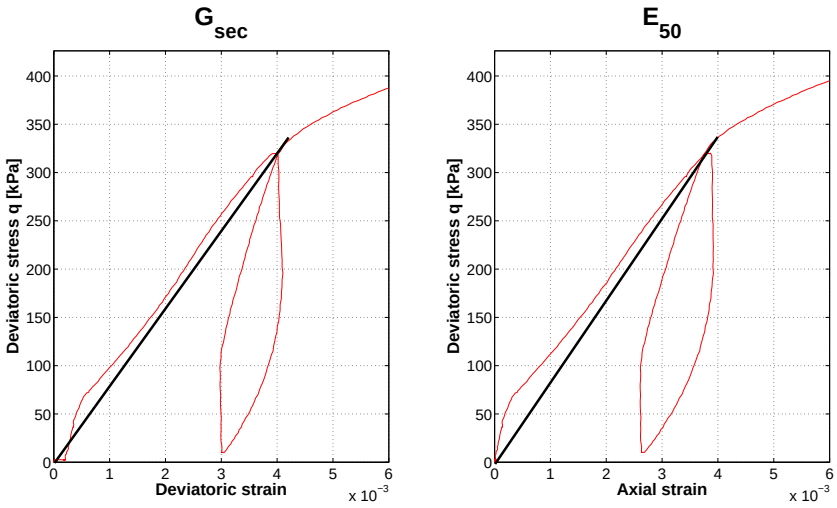

Figure 4.31: Young modulus E_{50} and shear modulus G_{sec} for Test 6 (CID).

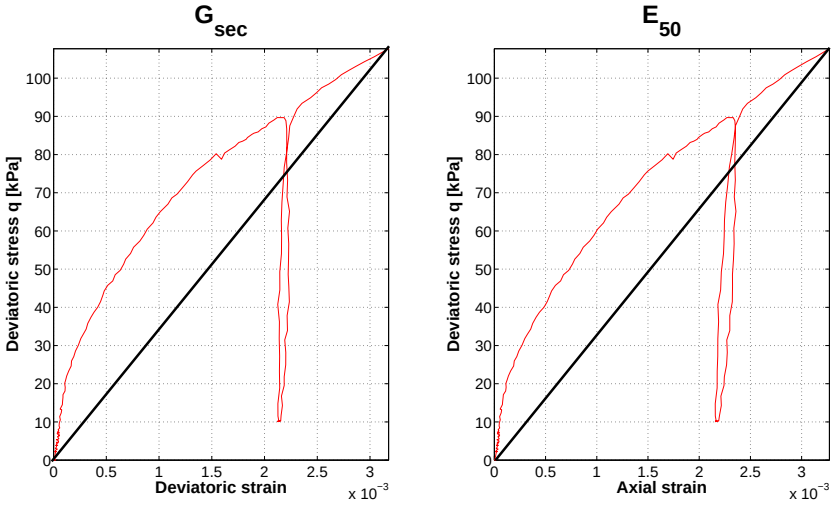

Figure 4.32: Young modulus E_{50} and shear modulus G_{sec} for Test 7 (CID).

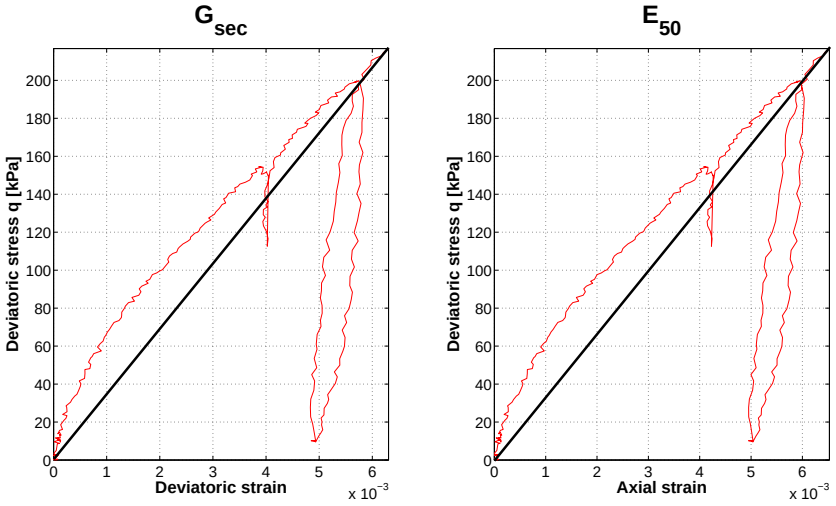

Figure 4.33: Young modulus E_{50} and shear modulus G_{sec} for Test 8 (CID).

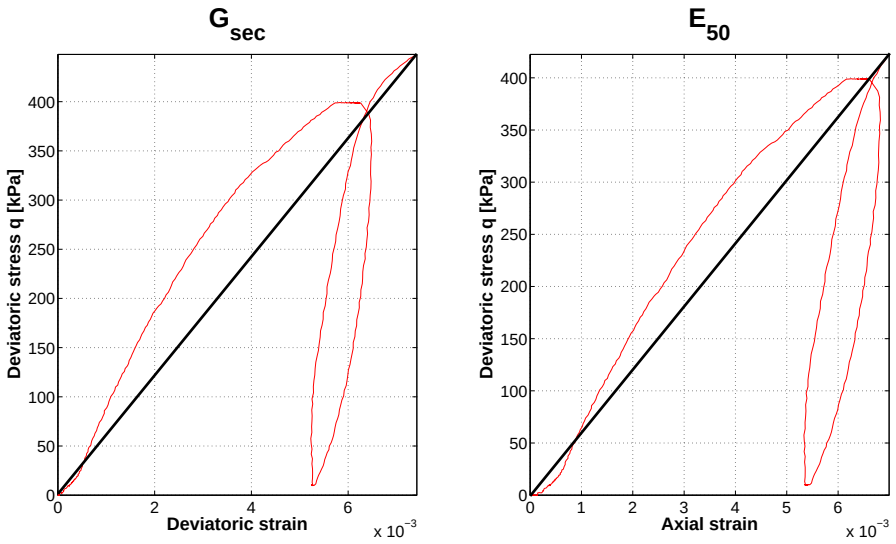

Figure 4.34: Young modulus E_{50} and shear modulus G_{sec} for Test 9 (CID).

Appendix D

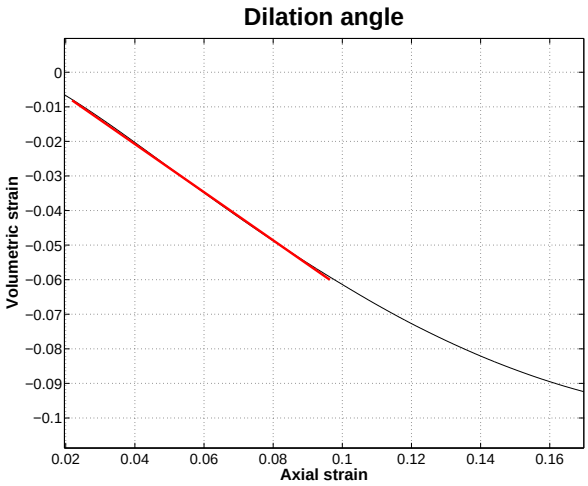

Figure 4.35: Dilation angle for Test 1 (CID).

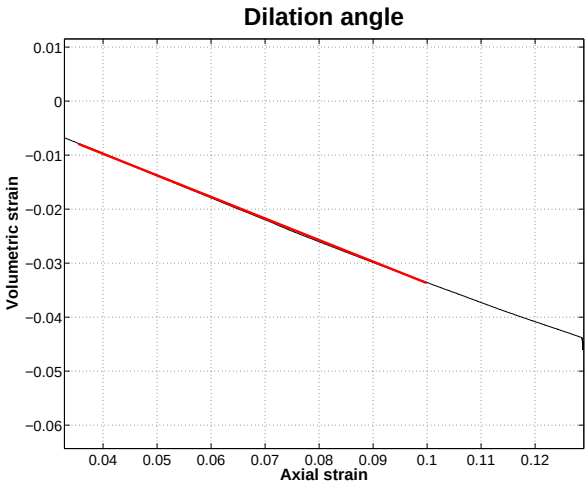

Figure 4.36: Dilation angle for Test 2 (CID).

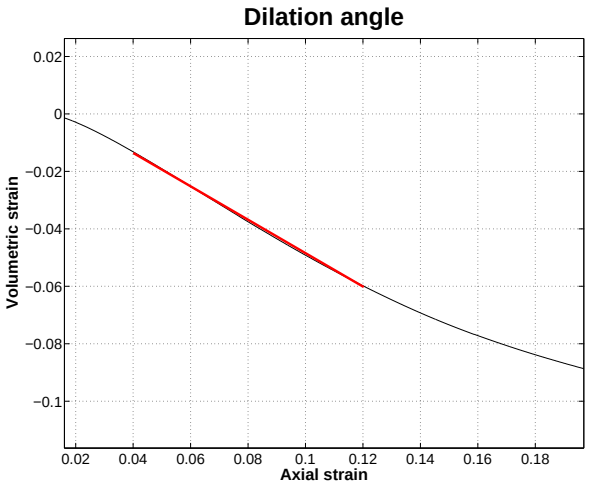

Figure 4.37: Dilation angle for Test 3 (CID).

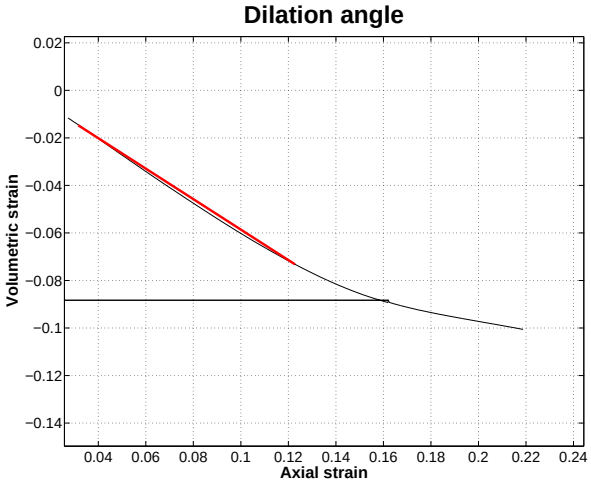

Figure 4.38: Dilation angle for Test 4 (CID).

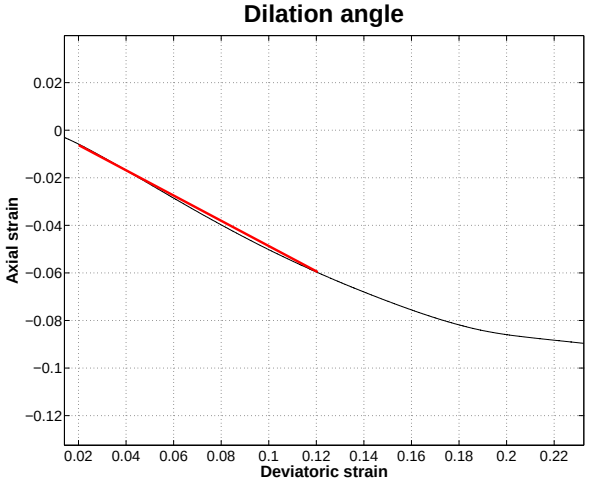

Figure 4.39: Dilation angle for Test 5 (CID).

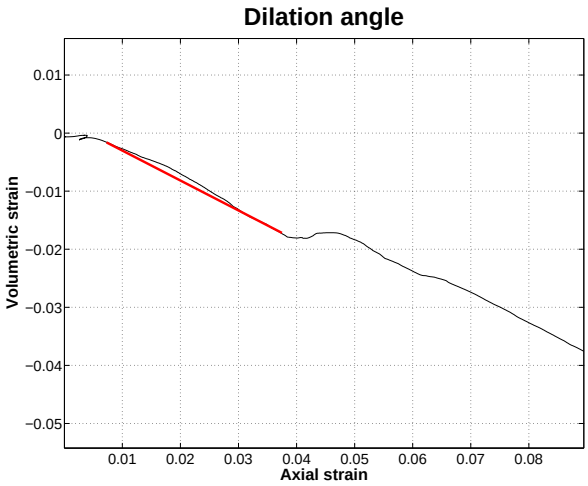

Figure 4.40: Dilation angle for Test 6 (CID).

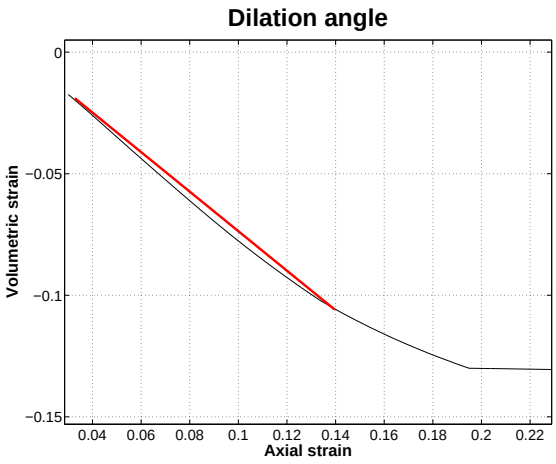

Figure 4.41: Dilation angle for Test 7 (CID).

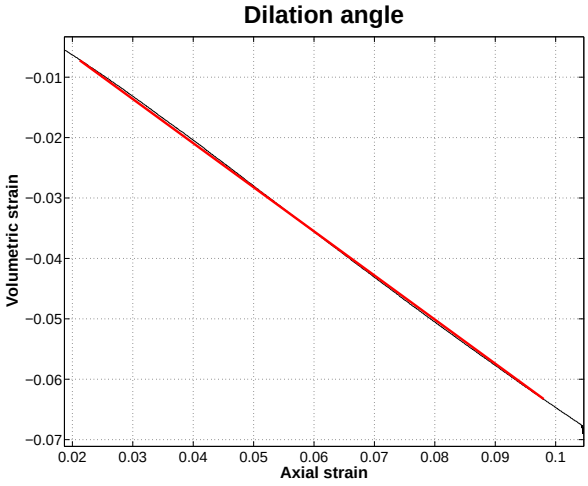

Figure 4.42: Dilation angle for Test 8 (CID).

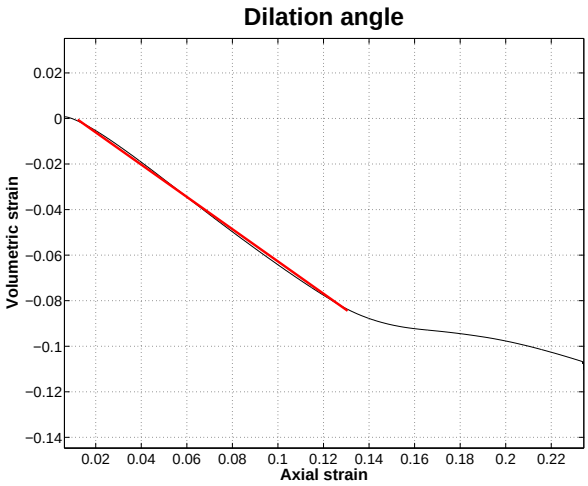

Figure 4.43: Dilation angle for Test 9 (CID).